Structural Insight into the Unique Properties of Adeno-Associated Virus Serotype 9

Michael A. DiMattia,[a]* Hyun-Joo Nam,[a]* Kim Van Vliet,[a] Matthew Mitchell,[a] Antonette Bennett,[a] Brittney L. Gurda,[a]* Robert McKenna,[a] Norman H. Olson,[b] Robert S. Sinkovits,[b]* Mark Potter,[c] Barry J. Byrne,[c] George Aslanidi,[c] Sergei Zolotukhin,[c] Nicholas Muzyczka,[d] Timothy S. Baker,[b] and Mavis Agbandje-McKenna[a]

Department of Biochemistry and Molecular Biology, Center for Structural Biology, McKnight Brain Institute, College of Medicine, University of Florida, Gainesville, Florida, USA[a]; Department of Chemistry and Biochemistry and Division of Biological Sciences, University of California—San Diego, La Jolla, California, USA[b]; Department of Pediatrics and Powell Gene Therapy Center, Division of Cell and Molecular Therapy, College of Medicine, University of Florida, Gainesville, Florida, USA[c]; and Department of Molecular Genetics and Microbiology and Powell Gene Therapy Center, College of Medicine, University of Florida, Gainesville, Florida, USA[d]

Adeno-associated virus serotype 9 (AAV9) has enhanced capsid-associated tropism for cardiac muscle and the ability to cross the blood-brain barrier compared to other AAV serotypes. To help identify the structural features facilitating these properties, we have used cryo-electron microscopy (cryo-EM) and three-dimensional image reconstruction (cryo-reconstruction) and X-ray crystallography to determine the structure of the AAV9 capsid at 9.7- and 2.8-Å resolutions, respectively. The AAV9 capsid exhibits the surface topology conserved in all AAVs: depressions at each icosahedral two-fold symmetry axis and surrounding each five-fold axis, three separate protrusions surrounding each three-fold axis, and a channel at each five-fold axis. The AAV9 viral protein (VP) has a conserved core structure, consisting of an eight-stranded, β-barrel motif and the αA helix, which are present in all parvovirus structures. The AAV9 VP differs in nine variable surface regions (VR-I to -IX) compared to AAV4, but at only three (VR-I, VR-II, and VR-IV) compared to AAV2 and AAV8. VR-I differences modify the raised region of the capsid surface between the two-fold and five-fold depressions. The VR-IV difference produces smaller three-fold protrusions in AAV9 that are less "pointed" than AAV2 and AAV8. Significantly, residues in the AAV9 VRs have been identified as important determinants of cellular tropism and transduction and dictate its antigenic diversity from AAV2. Hence, the AAV9 VRs likely confer the unique infection phenotypes of this serotype.

A deno-associated viruses (AAVs) are small, nonenveloped, single-stranded DNA (ssDNA) viruses that belong to the *Dependovirus* genus of the *Parvoviridae* family (49). In the past few decades, recombinant AAVs have become promising vectors for therapeutic gene delivery due to their ability to package and express foreign genes in the absence of active cell division in a broad range of tissues (22, 23, 26, 76, 77) and do so without any associated pathogenicity (6, 20). Despite these advantages, significant challenges remain in using AAV as a vector in the clinical setting owing to difficulties in delivering genes efficiently to target tissues, achieving long-term expression of the corrective transgene, and avoiding the detrimental effects of the host immune system. Twelve distinct AAV serotypes (AAV1 to AAV12) from human and nonhuman primate sources are known, and numerous recombinant species have been isolated (1, 26). Sequence identities among the capsid proteins of the 12 serotypes range from ~55 to 60% (for example, between AAV4 and AAV5 and between these two serotypes and the others) to >99% (for example, between AAV1 and AAV6) (1, 26).

AAV9 is a human AAV serotype (26) that has greatly enhanced transduction efficiency in cardiac and skeletal muscle, liver and pancreatic tissue, and the eye relative to other serotypes (e.g., see references 21, 31, 32, 54, 55, 69, and 70). Similar to other AAVs, AAV9 can transduce nondividing cells, including hepatocytes, which normally express factor IX (FIX). In hemophilia B studies, AAV9 vectors expressing FIX were able to transduce the liver without proinflammatory cytokine induction, unlike when similar experiments were performed with lentiviral vectors (71). Given its tissue tropism, AAV9 is being developed for a number of therapeutic gene delivery applications, for example, cardiac (21, 32,

69, 70, 76, 77) and ocular (40, 67) diseases, and blood coagulation disorders such as hemophilia A and B (16, 64) (Table 1). AAV9 can also cross the blood-brain barrier, and among all of the AAVs, it targets the central nervous system with high efficiency (24). Recently, a single intravenous injection of AAV9 vectors expressing α-*N*-acetylglucosaminidase (NAGLU) in mice with mucopolysaccharidosis IIIB (MPS IIIB; lysosomal storage disease) led to correction of their lysosomal storage pathology in the central and peripheral nervous systems and correction of astrocytosis and neurodegeneration (25). Given these properties, AAV9 is currently under development for treatment of neurodegenerative diseases, such as spinal muscle atrophy, amyotrophic lateral sclerosis, Parkinson's disease, and MPS IIIB (7, 25, 29, 30, 45, 80) (Table 1). Furthermore, while preexisting antibodies to AAVs have been shown to be detrimental to AAV gene delivery, the

TABLE 1 AAV9 tissue transduction properties

Tissue(s) transduced	Disease target(s)[a]	References
Cardiac and skeletal muscle	Virus-induced cardiomyopathy (targeting coxsackievirus B3 polymerase); RNAi strategies targeting phospholambin for treatment of heart failure; cardiac expression of anti-inflammatory mediators for autoimmune myocarditis; Pompe disease (glycogen storage disease type II)	21, 32, 69, 70
Eye	Retinal outer plexiform layer (OPL)	40
	Cornea	67
Liver (hepatocytes)	Factor IX (FIX) for blood coagulation disorders, such as hemophilia	16, 64
Brain and central nervous system	Transduction of motor neurons in neonate and adult animals; development for the treatment of spinal muscle atrophy, ALS, Parkinson's disease, and MPS IIIB (lysosomal storage disease); traverses the blood-brain barrier for delivery of therapeutics	18, 24, 25, 30, 34, 80

[a] RNAi, RNA interference; ALS, amyotrophic lateral sclerosis.

prevalence of antibodies to AAV9 is lower in humans than those of other serotypes, for example, AAV1 and AAV2 (8), making this serotype an even more attractive candidate for development as a gene delivery vector.

The AAV capsid contains 60 copies (in total) of three VPs that are encoded by the *cap* gene and have overlapping sequences. These include VP1 (87 kDa), VP2 (73 kDa), and VP3 (62 kDa), which are present in a predicted ratio of 1:1:10, respectively. The entire sequence of VP3 is contained within VP2, and all of VP2 is contained within VP1, which has a unique N-terminal (VP1u) domain. Only the common VP3 region is observed in all of the capsid structures of AAV serotypes determined to date, either by cryo-electron microscopy (cryo-EM) and image reconstruction (cryo-reconstruction) or by X-ray crystallography (27, 39, 41, 50, 51, 53, 56, 72, 78, 79). Comparisons of the AAV structures show that the core of each VP contains an eight-stranded β-barrel motif (βB to βI) and an α-helix (αA) that are also conserved in autonomous parvovirus capsids. Structurally variable regions (VRs) occur in the surface loops that connect the β-strands, which cluster to produce local variations in the capsid surface. Differences in the conformations of the VRs are predicted to dictate the variability of cellular tropism (both *in vitro* and *in vivo*), tissue transduction efficiency, and antigenic reactivity that is observed among the serotypes (27, 41, 51, 53, 72, 78, 79). These likely facilitate differential recognition of cell surface glycans and/or tissue-specific protein/lipid coreceptors for internalization or subsequent events in the AAV life cycle that lead to successful infection and transduction (1, 44, 61, 62). For some AAVs, the primary glycan receptor is cell surface heparan sulfate (HS), and for others, sialic acid and glycoprotein as well as glycolipid coreceptors have also been reported (reviewed in reference 1). For AAV9, terminal galactose is the primary receptor (4, 68) and the 37- to 67-kDa laminin receptor (LamR) was reported to play a role in its transduction (2).

Here we report structure determinations of the AAV9 capsid to 9.7- and 2.8-Å resolutions using the complementary approaches of cryo-reconstruction and X-ray crystallography, respectively. These studies were initiated to identify VRs on the surface of AAV9 that might be responsible for its enhanced tissue transduction compared to those of other AAV serotypes. The AAV9 cryo-reconstruction revealed and the higher-resolution X-ray crystal structure confirmed that VR-I and VR-IV adopt surface loop conformations in AAV9 that are unique compared to those of AAV2,

AAV3b, AAV4, AAV6, and AAV8, for which high-resolution crystal structures are available (27, 41, 51, 53, 78, 79). Significantly, VR-I and VR-IV amino acids as well as other VR regions have been reported to control the transduction phenotype in AAV1, AAV2, AAV6, and AAV8 (44) as well as AAV9 (37, 43, 60). VR-I is also part of an AAV2 and AAV3b conformational epitope (44, 74). These observations support previous suggestions that serotype-specific sequences and VR conformations help determine tropism, transduction efficiency, and antigenic reactivity for each AAV serotype (27, 44, 53). Comparison of the AAV9 VP3 crystal structure to those of other serotypes shows a difference at VR-II that is consistent with the flexible nature of the top of the DE loop that forms the five-fold channel in the parvovirus capsid.

MATERIALS AND METHODS

Virus capsid production and purification for structural analysis. Recombinant AAV9 virus-like particles (VLPs) were expressed using the Bac-to-Bac baculovirus-Sf9 insect cell expression system (Gibco/Invitrogen, Carlsbad, CA) and purified using a 20% sucrose cushion followed by a sucrose gradient (5 to 40% [wt/vol]) as previously reported (48). Purified AAV9 VLPs were concentrated to ~5 mg/ml (in 10 mM Tris-HCl [pH 7.5], 350 mM NaCl, and 2 mM MgCl$_2$, buffer A) using Apollo concentrators (Orbital Biosciences, LLC, Topsfield, MA) (150,000-molecular-weight cutoff) at 2,372 × g at 277 K and stored at the same temperature. Prior to use, the purity and integrity of the VLPs were monitored by SDS-PAGE and negative electron microscopy (EM), respectively. For the EM visualization, samples were negatively stained with 2% uranyl acetate and viewed on a JEOL JEM-100CX II electron microscope (48).

Cryo-EM of AAV9 VLPs. Small aliquots (3.5 μl) of purified AAV9 VLPs (~5 mg/ml in buffer A) were applied to glow-discharged EM grids that had a continuous-carbon film. The grids and sample were blotted with filter paper and plunged into ethane cooled to liquid with liquid nitrogen (93 K). The grids were transferred into liquid nitrogen, loaded into precooled sample cartridges, and subsequently placed into the microscope that was maintained at the liquid nitrogen temperature. The VLPs were viewed with an FEI Tecnai G2 Polara transmission electron microscope under low-dose conditions (~21 e⁻/Å^2) and operating at an acceleration voltage of 200 keV. Micrographs were recorded on a Gatan Ultrascan 4000, 4,000-by-4,000, charge-coupled device (CCD) camera (15-μm pixel size), which, at a calibrated magnification of ~80,000 resulted in a pixel size of 1.88 Å at the specimen.

Cryo-reconstruction of AAV9 VLPs. One hundred-fifty micrographs, exhibiting minimal specimen drift and astigmatism and recorded at underfocus settings of between 1.2 and 4.5 μm, were used for the image reconstruction. RobEM (cryoem.ucsd.edu/programs.shtm) was used to extract individual particle images and to preprocess them as described

elsewhere (3). The RMC (random-model computation) procedure (81) was used to generate an initial reconstructed model at an approximately 30-Å resolution from 150 particle images. This map was used to initiate full determinations of the orientations and origins of all particles and refinement of the entire set of images using the AUTO3DEM software package (82). Corrections to compensate for the effects of the microscope contrast transfer function were performed as described elsewhere (9, 83). A final three-dimensional (3D) map, reconstructed from 5,800 particle images, was estimated to be reliable to at least a 9.8-Å resolution based on a Fourier shell correlation (FSC) threshold criterion of 0.5. To aid the analysis and interpretation of the structure, an inverse temperature factor of 1/500 Å^2 was used to enhance the high-resolution features out to a 9.7-Å resolution (28). To prevent the amplification of noise in addition to the desired signal, the Fourier amplitudes were multiplied by a noise suppression factor of the form $C_{ref} = \sqrt{2FSC/(1 + FSC)}$ (63).

Model building into the AAV9 cryo-reconstruction. Prior to the structure determination of the AAV9 capsid structure by X-ray crystallography, a pseudoatomic model of residues 217 to 736 for the AAV9 VP3 subunit was generated to aid in interpreting the reconstructed density map. The model was built with the SWISS MODEL online model generator (http://www.expasy.org) (33, 66) for the AAV9 VP3 amino acid sequence (NCBI accession no. AAS99264.1) using the coordinates of the AAV2 (Protein Data Bank [PDB] accession no. 1LP3) and AAV8 (PDB accession no. 2QA0) crystal structures supplied as templates. These coordinates were used in addition to the docking of the AAV9 VLP crystal structure for interpretation of the cryo-reconstructed density map so we could compare the final pseudoatomic model derived in this way to the structure determined by X-ray crystallography (described below). The unique region of VP1, the common region between VP1 and VP2, and the extreme N-terminal end of VP3 were not included in the pseudoatomic model of AAV9 because there is presently no structural information available for these regions. A complete AAV9 capsid model, including 60 identical copies of the VP3 model, was generated by utilizing the standard icosahedral matrices (oligomer generator) within the VIPER database (14). The program SITUS (75) was used to dock both the capsid homology model and the crystal structure into the reconstructed AAV9 density map. The magnification of the cryo-EM density map was calibrated against the capsid coordinates by varying the pixel size of the map and choosing the size that yielded the highest real-space correlation coefficient as determined by the SFALL and FFT subroutines within CCP4 (17) and the shape similarity index subroutine within MAPMAN (35). At this stage, two surface loops in the AAV9 homology model (VR-I and VR-IV) protruded outside the EM density envelope, thereby indicating that the model did not reflect the actual conformations of these VRs. Hence, we computed a difference map (not shown) by subtracting the density for the homology model from the experimental AAV9 map and used this to manually readjust and remodel the exposed surface loops followed by real-space refinement using the Coot program (19). A final difference map ($F_o - F_c$) was calculated by subtracting the structure factors of the docked crystal structure from those of the cryo-EM map.

Computing low-resolution structures of AAV2, AAV4, and AAV8 capsids to compare to the AAV9 cryo-reconstruction. The crystal structures of AAV2, AAV4, and AAV8 (27, 51, 78) were used to generate density maps at a 9.7-Å resolution as previously described (5) from structure factor amplitudes and phases derived from the atomic coordinates. Briefly, the SFALL and FFT subroutines of CCP4 (17) were used, respectively, to calculate structure factors to the desired resolution from atomic coordinates of the complete 60-VP capsid and to generate a density map. The maps were rendered for viewing in Chimera (59) and color cued by radius to highlight the surface topologies of the different AAV capsids at the resolution of the cryo-reconstruction.

X-ray crystallography of AAV9 VLPs (i) Crystallization, data collection, data reduction, and molecular replacement. Crystallization of AAV9 VLPs and preliminary characterization of the diffraction data (at ~2.8-Å resolution) for the crystals, including space group (P3$_2$) determi-

TABLE 2 Data collection and processing statistics

Parameter	Value for parameter[a]
Data collection (CHESS[f] F1)	
Wavelength, λ (Å)	1.0809
Space group	P3$_2$
Unit cell dimensions, $a = b$, c (Å)	250.68, 632.92
Resolution range (Å)[a]	40–2.8 (2.9–2.8)
No. of unique reflections	1,039,725 (80,399)
Completeness (%)	95.1 (73.6)
Avg $I/\sigma\langle I\rangle$	15.4 (2.9)
R_{merge} (%)[b]	15.5 (42.2)
Refinement (CNS version 1.3)[c]	
No. of atoms (protein/solvent/DNA)	4,130/58/0
Avg protein B factors (Å^2) (solvent)	43.39 (38.44)
R_{work}/R_{free} (%)[d]	28.27/28.21
RMSD[e]	
Bond length (Å)	0.0076
Bond angle (°)	1.44
Ramachandran plot (%)	
Most favorably allowed regions	95.3
Additionally allowed regions	4.3

[a] Values in parentheses are for the highest resolution.
[b] $R_{merge} = \Sigma|I_{hkl} - \langle I_{hkl}\rangle|/\Sigma|I_{hkl}| \times 100$, where I_{hkl} is the intensity of an individual hkl reflection and $\langle I_{hkl}\rangle$ is the mean intensity for all measured values of this reflection. The summation is over all equivalent intensities.
[c] CNS, Crystallography and NMR System (12).
[d] $R_{work} = \Sigma||F_o| - |F_c||/\Sigma|F_o| \times 100$, where F_o represents the observed structure factor amplitudes and F_c represents the structure factor amplitudes calculated from the atomic model. R_{free} was calculated with the 5% of reflections excluded from the data set during refinement.
[e] RMSD, root mean square deviation.
[f] Cornell High Energy Synchrotron Source.

nation, has been reported previously (48). Also, the orientation and position of the AAV9 VLPs in the P3$_2$ unit cell were previously determined (48) in a molecular replacement procedure using the program AMoRe (52). The initial phasing model for the AAV9 structure determination was a 60-mer generated from the coordinates of the AAV8 VP3 capsid subunit (PDB identification [ID] no. 2QA0) (51).

(ii) Crystallographic structure determination and refinement. The structure of AAV9 VLPs was determined from the crystals obtained with ammonium sulfate [(NH$_4$)$_2$SO$_4$] as an additive (48). The structure refinement utilized the Crystallography and NMR System (CNS) program (12). The AAV8 VP3 monomer model was refined while constrained by 60-fold noncrystallographic symmetry (NCS). The first refinement cycle included simulated annealing, energy minimization, and individual temperature factor (B-factor) refinement (12). Following this procedure, 60-fold NCS-averaged, Fourier $2F_o - F_c$ and $F_o - F_c$ electron density maps (where F_o represents the observed structure factor amplitudes and F_c represents the structure factor amplitudes calculated from the atomic model) were generated, with a molecular mask comprising the VP3 monomer plus a 3-Å cushion, and used for model building in Coot (19). The AAV8 residues in the starting model were replaced with appropriate AAV9 residues using the SWISS-MODEL program (33), and the side-chains were adjusted as guided by the current, refined electron density map. This model building was followed by energy minimization and B-factor refinement using CNS. Cycles of interactive model building into averaged density maps followed by refinement were repeated until there was no further improvement in the R_{work} metric that is used to calculate the agreement between the observed structure factors and those calculated from the model following each round of building: $R_{work} = \Sigma|F_o| - |F_c|/\Sigma|F_o| \times 100$, where F_o and F_c are as defined above. Density map modification was also carried out in the final stages with the "density modification" subroutine in CNS (12). A test data set representing 5% of the total recorded reflections was partitioned
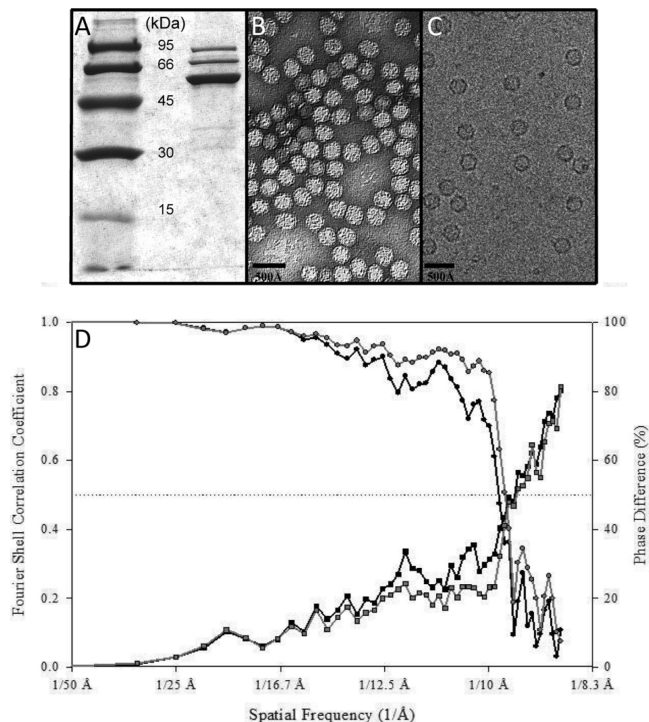
FIG 1 Characterization and cryo-EM of baculovirus-expressed AAV9 VLPs. (A) SDS-PAGE of AAV9 showing VP1, VP2, and VP3, which have masses of 87, 73, and 62 kDa, respectively. (B and C) Micrographs of negatively stained (B) and vitrified (C) AAV9 VLPs. Size marker, 500 Å. (D) Resolution estimation using Fourier shell correlation (FSC) coefficient values and average phase difference between two half-data sets plotted versus spatial frequency for the temperature factor corrected (gray) and uncorrected (black) structures. The resolution was determined to be where the average phase difference increases to 50% or the correlation coefficient dropped below 0.5, indicated by the horizontal dashed line.

for monitoring the refinement process and used to calculate R_{free} (same as R_{work} but calculated with just this 5% of the data) (11). Solvent molecules, within hydrogen bond donor or acceptor distances, and acceptable temperature (B) factors, were built into unassigned density at a 3.0-σ threshold in the final averaged $F_o - F_c$ electron density map. The quality of each refined VP3 structure was accessed using Coot and MolProbity (15, 19). Refinement statistics are listed in Table 2.

Comparison of AAV9 VP3 to other AAV structures. The refined AAV9 VP3 crystal structure was compared with the VP3 structures of AAV2 (PDB accession no. 1LP3), AAV4 (PDB accession no. 2G8G), and AAV8 (PDB accession no. 2QA0) by structural alignment with the SSM (Secondary Structure Matching) program (38).

Protein structure accession number. The refined coordinates and structure factors for the AAV9 structure have been deposited in the RCSB PDB database under accession no. 3UX1.

RESULTS AND DISCUSSION

Surface topology of the AAV9 capsid. A cryo-reconstruction of AAV9 was obtained from micrographs of vitrified samples of baculovirus-expressed VLPs propagated in Sf9 cells and purified by sucrose density ultracentrifugation (Fig. 1). A total of 5,800 boxed particle images were used to reconstruct the final 3D density map to 9.7-Å resolution (Fig. 1D and 2A). The AAV9 capsid shows surface features characteristic of other AAV serotypes. These include a depression at the icosahedral two-fold axis, three protrusions surrounding the three-fold axis, and a moat-like depression

that surrounds a central channel at the five-fold axis (Fig. 2A). A cross-sectioned view of the capsid shows density features corresponding to the βA strand as well as the βBIDG sheet of the conserved eight-stranded β-barrel motif that forms the core of the capsid subunit in all parvoviruses (Fig. 2B). Densities for two key features of the AAV surface are clearly resolved at 9.7-Å resolution: the DE loop (connect βD and βE strands) protrusions that form the central channel at each five-fold axis and the HI loops (connect βH and βI strands) that lie on the floor of the depression around each five-fold axis (Fig. 2A and C). The external diameter of the AAV9 capsid varies from a minimum of ~230 Å at the icosahedral two-fold axis and 250 Å at the three-fold and five-fold axes to a maximum of ~290 Å at the tips of the protrusions that are surrounding the three-fold axis and lie ~30 Å from that axis.

The 9.7-Å resolution structure of AAV9 was compared to density maps of the AAV2, AAV4, and AAV8 capsids computed to 9.7-Å resolution from their atomic coordinates (27, 51, 78) (Fig. 2A, D, E, and F). The two-fold depression is conserved in all four capsids, although the widths and shapes of these depressions differ slightly (Fig. 2). The three-fold protrusions of AAV9 differ from those of AAV2, AAV4, and AAV8 (Fig. 2). The "pointed finger-like" tips of the AAV2 (Fig. 2D) and AAV8 (Fig. 2F) protrusions are missing in AAV9 (Fig. 2A to C) and AAV4 (Fig. 2E). Differences in the structures of these protrusions among AAV2, AAV4, and AAV8 have been ascribed to variations in the conformations of surface loops (27, 51). AAV9 has shorter protrusions, indicating that the corresponding surface loops in the AAV9 VP3 subunit must adopt different conformations. Density at the base of each protrusion, which creates a raised surface region (a "two/five-fold wall") between the depressions at the two-fold axes and surrounding the five-fold axes, differs in all four serotypes. The DE loops are similarly arranged in AAV2, AAV8, and AAV9 but differ from those in AAV4 (Fig. 2), which is consistent with the difference that was previously reported for the VR-II regions of AAV2 and AAV4 (27). Density formed by the HI loop in all four serotypes is structurally conserved (Fig. 2).

The AAV9 pseudoatomic model built into reconstructed density reveals variable regions. The amino acid sequences of VP3 show that AAV9 is ~81% identical to AAV2, ~57% identical to AAV4, and ~83% identical to AAV8. The docking of a homology model built for AAV9 VP residues 217 to 736 (the VP3 common region) from AAV2 and AAV8 into the reconstructed density map showed that the surface loops comprising VR-I and VR-IV needed readjustment (away from the template orientation) to better fit surface features of the AAV9 capsid (Fig. 3A). Significantly, VR-I and VR-IV are among the most structurally diverse VRs characterized to date. The rest of the VP3 model fits the reconstructed density envelope with no further adjustment (Fig. 3A). For example, the conserved α-helical region (αA) that flanks the icosahedral two-fold axis in all parvovirus structures determined to date was clearly interpretable in the 9.7-Å cryo-EM map contoured at a threshold of 3.8 σ (not shown). The correlation coefficient between this pseudoatomic model and the cryo-reconstructed map, as calculated using the "fit in map" command in Chimera (59), was 0.94. When the AAV9 pseudoatomic model is compared with AAV2, AAV4, and AAV8, differences in the capsid topologies at the two/five-fold wall correlate with conformational differences in VR-I (Fig. 2A, C, D, and F). The conformation of VR-IV in each serotype leads to topological differences at the tops
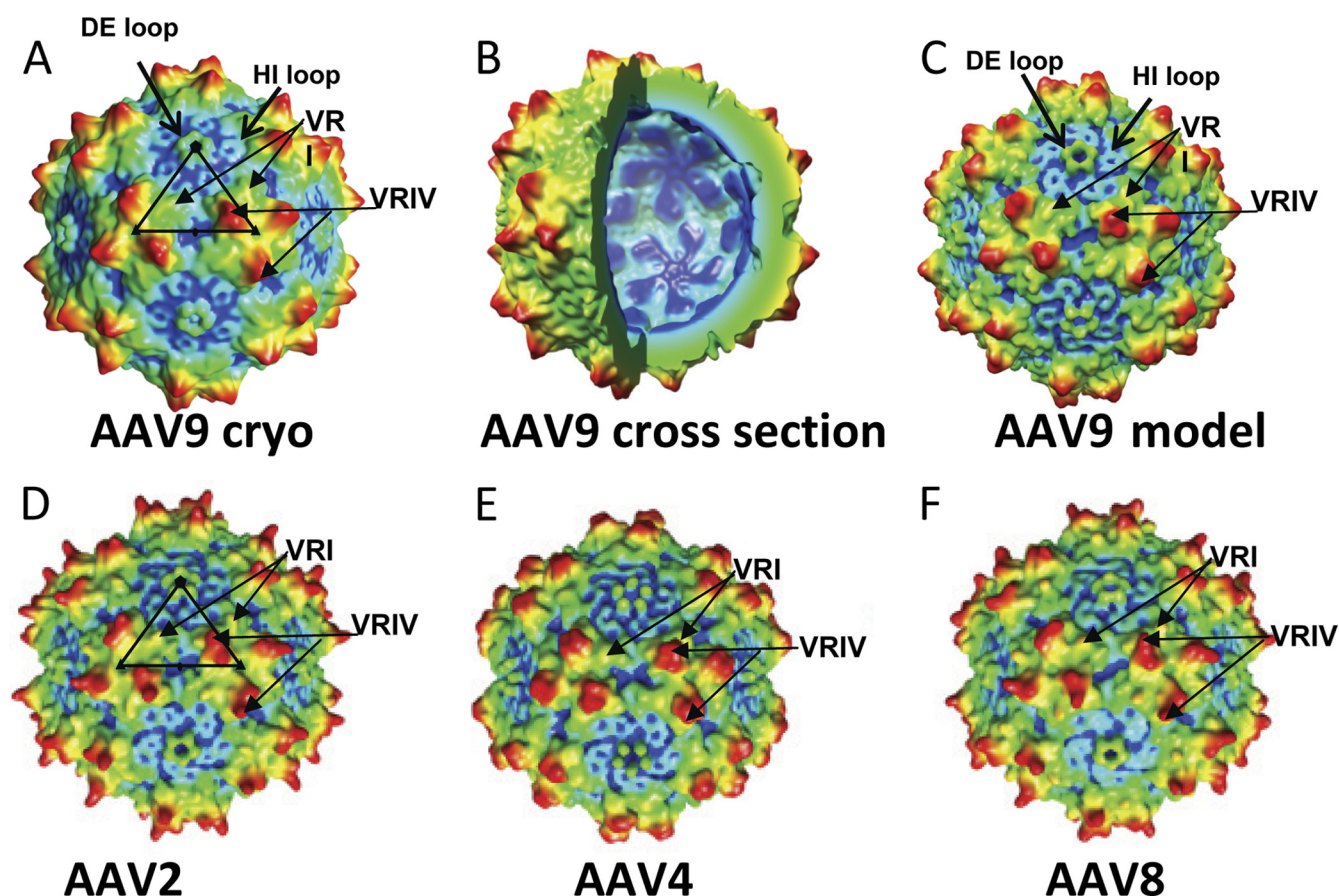
FIG 2 Comparison of AAV structures at a 9.7-Å resolution. (A) AAV9 cryo-EM density map. (B) Cross-section of the AAV9 cryo-EM density map with an octant removed to show the capsid interior. (C) A surface density map of the pseudoatomic model built into the AAV9 cryo-EM reconstructed density map. (D, E, and F) Surface density maps for AAV2, AAV4, and AAV8, respectively, generated from structure factors and phases calculated from atomic coordinates to a resolution of 9.7 Å. The capsid surfaces shown in panels A and C to F are radially depth cued with colors ramping from red, to yellow, to green, to cyan, and finally to dark blue. In panel B, the radial range for the depth cueing was expanded to enhance the internal surface features. All density maps are viewed down an icosahedral two-fold axis. The triangles in A and D depict a viral asymmetric unit bounded by a five-fold axis and two three-fold axes. Density for the DE and HI loops conserved in all parvovirus structures determined to date is indicated by arrows in A and C. Example capsid surface regions corresponding to VR-I and VR-IV are indicated by arrows in panels A and C to F. The images were generated using Chimera (59).

of the three-fold protrusion (Fig. 2A, C, D, and F). Of note, the 9.7-Å medium resolution of the AAV9 cryo-reconstruction is sufficient to identify two of the largest surface loop differences that had previously been reported based on comparison of the AAV2 crystal structure with those of AAV4, AAV6, and AAV8 (27, 51, 53).

The AAV9 crystal structure. To obtain detailed information on the position of amino acids in AAV9 VR-I and VR-IV as well as other potential VRs between AAV9 and other AAVs not resolved in the cryo-EM reconstruction, the structure was also determined by X-ray crystallography. The AAV9 structure, determined from crystals grown in the presence of $(NH_4)_2SO_4$, was refined to a 2.8-Å resolution. The final R_{work} and R_{free} values after restrained B value refinement were 28.27% and 28.21% (Table 2), respectively. The similarity between these values results from the noncrystallographic redundancy of the virus data set. The values are consistent with those reported for other AAV structures and within the range of values reported for other virus structures determined to comparable resolution, as documented in VIPERdb (http://viperdb .scripps.edu) (14).

The AAV9 crystal structure showed that residues 219 to 736

(VP1 numbering), all within the VP3 overlapping sequence, are ordered. As seen with other AAV (and most other parvovirus) structures, the VP1u and VP1/VP2 overlap regions and the first 16 N-terminal residues of VP3 are disordered and hence invisible in the averaged density map. This lack of electron density in the N-terminal VP regions could be due to inherent flexibility of the polypeptide region immediately preceding the ordered residues in all three VPs, which allows this region to adopt different conformations. In addition, the low copy numbers of the VP1 and VP2 unique regions mean that their signal in the density map will be diminished during the icosahedral averaging that is employed in the structure determination process.

The ordered AAV9 VP structure (here referred to as "VP3"), as predicted, has the conserved AAV structural topology, which includes the eight-stranded β-barrel (βB to βI), the αA helix, and loop insertions between the β-strands (Fig. 4A). In addition, the AAV9 crystal structure provided atomic detail that distinguishes it from the structures of AAV2, AAV4, and AAV8, including the differences at VR-I and VR-IV (Fig. 4B and C). Docking of the crystal structure into the cryo-reconstructed density (correlation coefficient of 0.98) showed these variable regions within the den-
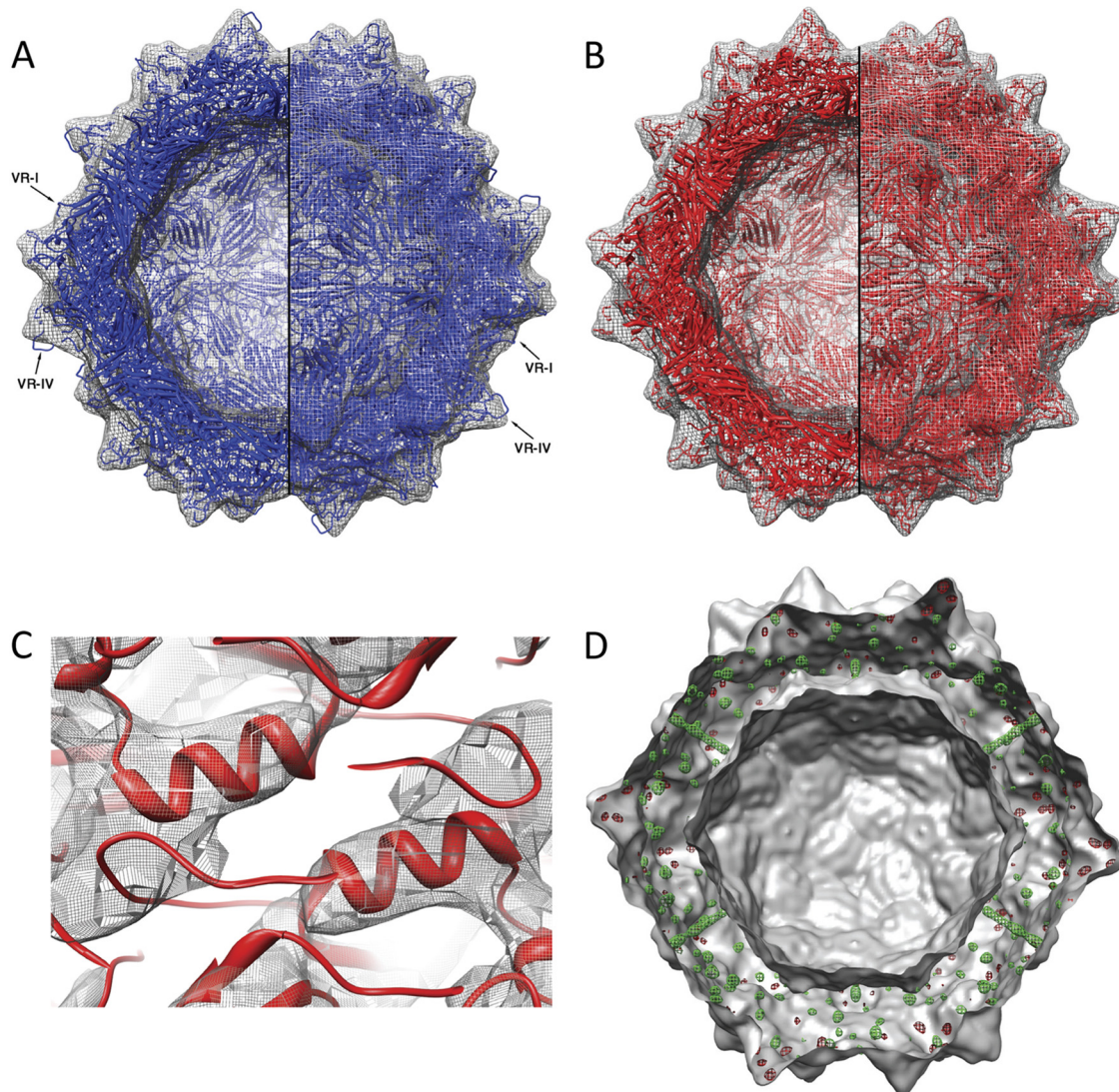
FIG 3 Modeling of the cryo-reconstructed AAV9 density map. (A) The AAV9 capsid pseudoatomic model (in blue) generated by SWISS MODEL (33) using the AAV2 and AAV8 crystal structures as templates. Two surface loops (VR-I) and (VR-IV) per capsid monomer required adjustment to fit within the cryo-EM density map (in gray mesh, contoured at 1.2 σ). The left half of the capsid is a cross-section to show the fit of the model in the capsid interior. (B) The AAV9 capsid crystal structure (in red) inside the cryo-EM map (in gray mesh; contoured at 1.2 σ). (C) The conserved α-helical region (αA) in the VP3 crystal structure shown inside the cryo-reconstructed density at a threshold of 3.8 σ. This region, which flanks the icosahedral two-fold axis in all parvovirus structures determined to date, was clearly resolved in the 9.7-Å-resolution cryo-reconstructed map. (D) Cross-section of an isosurface rendering (in gray) of the cryo-reconstruction overlaid with a difference map ($F_o − F_c$) calculated by subtracting the structure factors of the docked crystal structure from those of the cryo-EM map. Positive difference density is shown in green; negative difference density is shown in red. The positive tubular density is inside the five-fold channel. The images were generated using Chimera (59).

sity envelope without need of adjustment, unlike the homology model generated from AAV2 and AAV8 (Fig. 3A and B). As with the model, the conserved α-helix in the crystal structured docked into the cryo-reconstructed density without adjustment (Fig. 3C). A difference map calculated by subtracting the crystal structure from the AAV9 cryo-reconstruction ($F_o − F_c$, as defined above) revealed small "blobs" of positive density inside the capsid and a stretch of positive density inside the five-fold channel at a density threshold of 6.0 σ (Fig. 3D). Small patches of negative difference density were also observed close to the capsid surface regions (Fig. 3D), consistent with the high thermal motion in the atomic coordinates for constituent residues, as indicated by high B-factors.

Given the resolution of the map, these different densities were not modeled; however, positive density within the five-fold channel has been observed for other parvoviruses, including AAV8 (51). These observations and biochemical data support the hypothesis that it is the five-fold channel through which VP1u is externalized, thereby facilitating its phospholipase A2 (PLA2) activity and nuclear targeting.

Topological differences in the AAV9 capsid are consistent in the cryo-EM and X-ray density maps. The structures of the surface VRs in different AAV serotypes are what primarily dictate serotype- or strain-specific functions (27). Alignment and superposition of the AAV9 VP3 structure with the known crystal struc-
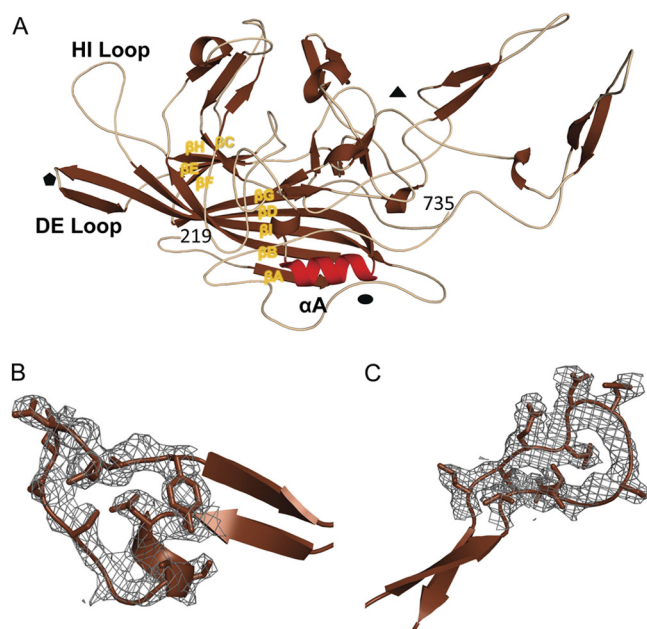
FIG 4 The AAV9 VP3 crystal structure. (A) AAV9 monomer indicating the conserved eight-stranded β-barrel motif present in all parvovirus capsids, as well as the conserved αA at the two-fold symmetry axis. Small regions of β-strand and α-helical structure are present in the loop regions between the β-barrel strands. The approximate positions of the icosahedral two-, three-, and five-fold axes are indicated with filled oval, triangle, and pentagon symbols, respectively. (B) Close-up view of VR-I and (C) VR-IV showing $2F_o - F_c$ density (contoured at a threshold of 1.5 σ) for the side chain atoms in these surface loops. The images were generated using PyMol (the PyMOL Molecular Graphics System version 1.3, Schrödinger, LLC.).

tures of AAV2, AAV4, and AAV8 showed that it differs most in structure from AAV4 and is more similar to AAV2 and AAV8, just as was predicted from the cryo-EM structure (Fig. 2, 5, and 6). AAV9 and AAV4 differ at all of the nine AAV VRs defined when comparing AAV2 and AAV4 (27), and AAV9 differs from AAV2 and AAV8 at VR-I, VR-II, and VR-IV (Fig. 6A to D). The conformational differences in these three VRs are located at residues 262 to 269 (VR-I, AAV9 VP1 numbering), 327 to 332 (VR-II), and 452 to 460 (VR-IV) in the AAV9 VP3 crystal structure. AAV9 VR-I contains 2- and 5-aa residue insertions relative to AAV2 and AAV4, respectively, and no deletions or insertions relative to AAV8 (Fig. 5). AAV9 VR-IV has a single amino acid residue insertion relative to AAV2 and AAV8 and two fewer amino acid residues than AAV4. No insertions or deletions are responsible for the loop differences seen in VR-II. The other AAV9 VRs, VR-III, VR-V, VR-VI, VR-VII, VR-VIII, and VR-IX (Fig. 5) are defined as variable based on the comparison with AAV4 showing differences in the Cα positions of >1.0 Å for two or more residues (27, 36). When AAV9 is compared to AAV2 and AAV8 at these VP regions, the Cα positions differ by <1.0 Å, although there are differences in amino acid residue type (Fig. 5).

Variable regions I to IX contribute to the surface features of the AAV capsid and result in topological differences (reviewed in references 1, 57, and 73), as already described above for VR-I and VR-IV. Variable regions VR-IV, VR-V, and VR-VIII assemble the top of the protrusions surrounding the three-fold axis, and VR-I, VR-III, and VR-VII form the surface of the two/five-fold wall (Fig. 2, 6A, and 7). VR-IX is also on the two/five-fold wall but close to

the two-fold depression (Fig. 6A). AAV9 VR-II is located at the top of the five DE loops that form the channel at each five-fold vertex (Fig. 6). Of note, while the homology model built into the cryo-EM reconstructed density did not predict the AAV9 VR-II difference from AAV4, this variation is evident when the surface topologies of the two serotypes are compared at a 9.7-Å resolution (Fig. 2). The flexibility of VR-II is typical for the parvoviruses (27, 36). This flexibility is believed to facilitate externalization of VP1u through the five-fold channel to perform its PLA2 function during cellular trafficking, as reviewed in references 1, 57, and 73. The five-fold channel is furthermore proposed to act as the portal through which DNA is packaged after the capsid assembles (reviewed in reference 1). The HI loop, which lines the floor of the depression around the five-fold channel, is structurally conserved among AAV2, AAV4, AAV8, and AAV9 (Fig. 6A), consistent with a reported role in genome packaging for the AAVs (1, 57, 73). The conservation of this loop was also observed in the 9.7-Å resolution cryo-reconstructed map.

AAV9 VRs are associated with receptor attachment, transduction efficiency, and antigenic diversity. Past comparative studies of AAV VPs showed that sequence and local structural differences likely dictate the variations observed in tissue tropism, transduction efficiency, and antigenicity between the serotypes (1, 2, 27, 41, 44, 51, 53, 60–62, 79). While the site on the AAV9 capsid that binds galactose has yet to be identified, residues 489 to 545 and 591 to 621 (AAV9 VP1 numbering) in the VRs within the GH loop (located between the βG and βH strands; Fig. 5) map to the footprint for the interaction between AAV8 and the LamR receptor, which is also reported to be utilized by AAV2, AAV3, and AAV9 (2) (Fig. 7). The first stretch of residues overlaps with amino acids in VR-V and VR-VI, whereas the second stretch contains residues within VR-VIII and conserved amino acids located just before the βH strand (Table 3 and Fig. 5). Among AAV2, AAV8, and AAV9, there are residue differences in VR-V, VR-VI, and VR-VIII, but the structures are similar at these VRs (Fig. 5, 6, and 7). This suggests that it may be the capsid region around the three-fold axis rather than specific sequence that dictates how these AAVs recognize LamR, or perhaps the conserved second stretch of residues (591 to 621) located closer to the three-fold axis (Fig. 7) may be the major recognition determinant.

Several studies have also shown that VR residues in AAV9 are important determinants of cellular tropism and transduction (Table 3) (37, 43, 60). For example, site-directed mutagenesis demonstrated that VR-V residues 503 and 504 affect liver- and muscle-specific transduction in AAV9 (60). Residue Trp503 is conserved in AAV2, AAV8, and AAV9, but not in AAV4, where it is an isoleucine, and residue 504 is a proline in AAV9, a threonine in AAV2 and AAV8, and a lysine in AAV4 (Fig. 5). Thus, the capsid surface containing these residues likely engages in tissue-specific interactions that are not possible for the other serotypes. Another study, on AAV1/9 chimeric capsids, identified amino acids in VR-IV (aa 456 to 476) and VR-VII (aa 550 to 568) (Fig. 5) as determinants of AAV9's increased liver transduction efficiency compared to AAV1 (37). The study by Kotchey et al. (37) also identified AAV9 aa 699 to 735 (contains VR-IX) (Fig. 5) as being important for heart tropism. The backbone of VR-IX is structurally conserved between AAV2, AAV8, and AAV9 (Fig. 6) as well as AAV1 (data not shown; L. Govindasamy and M. Agbandje-McKenna, unpublished data) but contains sequence and side chain structure differences (Fig. 5) (data not shown) at positions 706, 709, 710, and 712
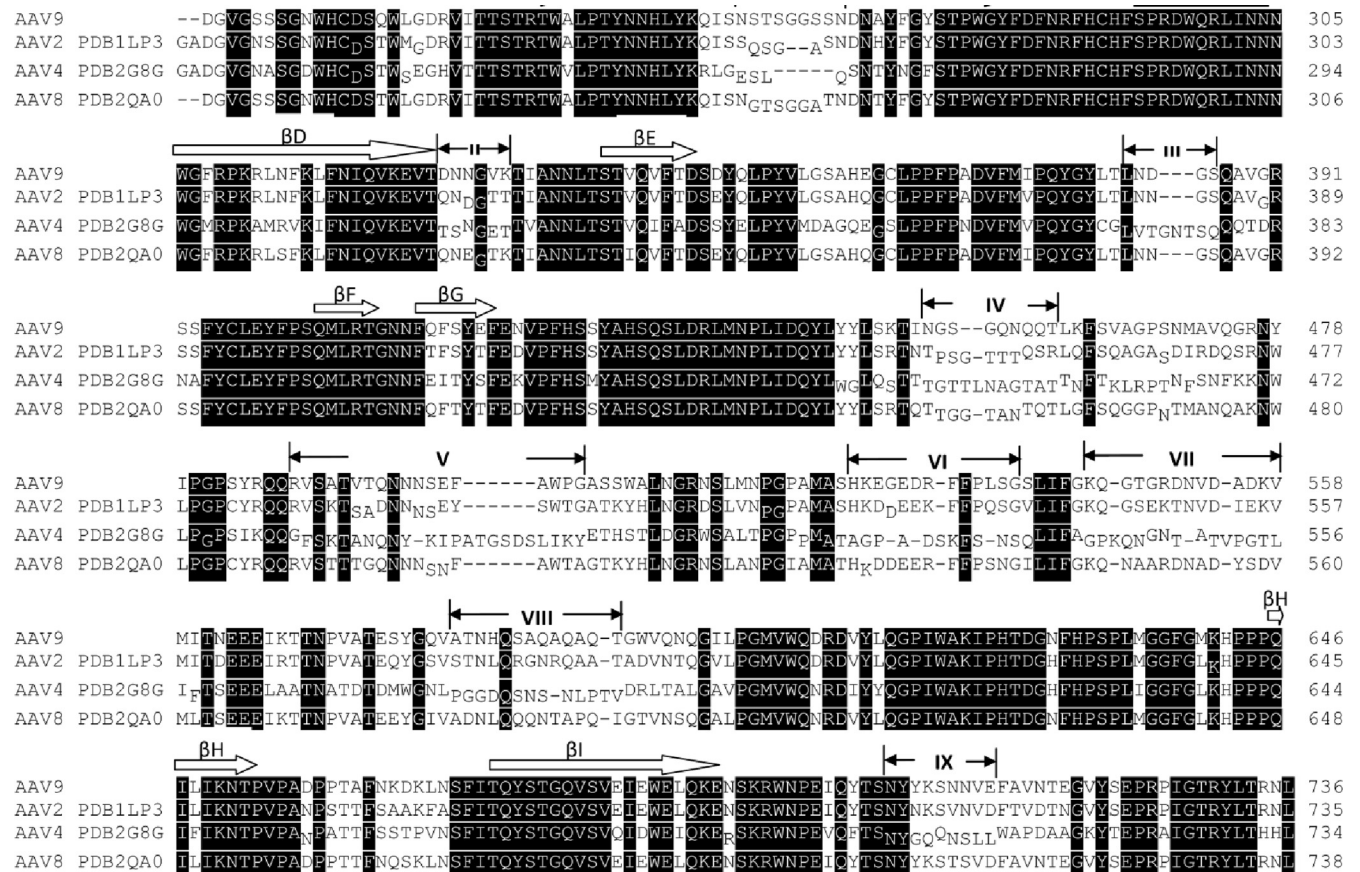
```
                                                                                                              βD              II                    βE                                              III
AAV9              --DGVGSSGNWHCDSQWLGDRVITTSTRTWALPTYNNHLYKQISNSTSGGSSNDNAYFGYSTPWGYFDFNRFHCHFSPRDWQRLINNN  305
AAV2 PDB1LP3      GADGVGNSSGNWHCDSTWMGDRVITTSTRTWALPTYNNHLYKQISSQSG--ASNDNHYFGYSTPWGYFDFNRFHCHFSPRDWQRLINNN  303
AAV4 PDB2G8G      GADGVGNASGDWHCDSTWSEGHVTTSTRTWVLPTYNNHLYKRLGESL-----QSNTYNGFSTPWGYFDFNRFHCHFSPRDWQRLINNN   294
AAV8 PDB2QA0      --DGVGSSGNWHCDSTWLGDRVITTSTRTWALPTYNNHLYKQISNGTSGGATNDNTYFGYSTPWGYFDFNRFHCHFSPRDWQRLINNN   306

AAV9              WGFRPKRLNFKLFNIQVKEVTDNNGVKTIANNLTSTVQVFTDSDYQLPYVLGSAHEGCLPPFPADVFMIPQYGYLTLND---GSQAVGR  391
AAV2 PDB1LP3      WGFRPKRLNFKLFNIQVKEVTQNDGTTTIANNLTSTVQVFTDSEYQLPYVLGSAHQGCLPPFPADVFMVPQYGYLTLNN---GSQAVGR  389
AAV4 PDB2G8G      WGMRPKAMRVKIFNIQVKEVTSNGETTVANNLTSTVQIFADSSYELPYVMDAGQEGSLPPFPNDVFMVPQYGYCGLVTGNTSQQTDR    383
AAV8 PDB2QA0      WGFRPKRLSFKLFNIQVKEVTQNEGTKTIANNLTSTIQVFTDSEYQLPYVLGSAHQGCLPPFPADVFMIPQYGYLTLNN---GSQAVGR  392

                                        βF        βG                                               IV                V
AAV9              SSFYCLEYFPSQMLRTGNNFQFSYEFENVPFHSSYAHSQSLDRLMNPLIDQYLYYLSKTINGS--GQNQQTLKFSVAGPSNMAVQGRNY  478
AAV2 PDB1LP3      SSFYCLEYFPSQMLRTGNNFTFSYTFEDVPFHSSYAHSQSLDRLMNPLIDQYLYYLSRTNTPSG-TTTQSRLQFSQAGASDIRDQSRNW  477
AAV4 PDB2G8G      NAFYCLEYFPSQMLRTGNNFEITYSFEKVPFHSMYAHSQSLDRLMNPLIDQYLWGLQSTTTGGTTLNAGTATTNFTKLRPTNFSNFKKNW 472
AAV8 PDB2QA0      SSFYCLEYFPSQMLRTGNNFQFTYTFEDVPFHSSYAHSQSLDRLMNPLIDQYLYYLSRTQTTGG-TANTQTLGFSQGGPNTMANQAKNW  480

                                        VI              VII
AAV9              IPGPSYRQQRVSATVTQNNNSEF------AWPGASSWALNGRNSLMNPGPAMASHKEGEDR-FFPLSGSLIFGKQ-GTGRDNVD-ADKV  558
AAV2 PDB1LP3      LPGPCYRQQRVSKTSADNNNSEY------SWTGATKYHLNGRDSLVNPGPAMASHKDDEEK-FFPQSGVLIFGKQ-GSEKTNVD-IEKV  557
AAV4 PDB2G8G      LPGPSIKQQGFSKTANQNY-KIPATGSDSLIKYETHSTLDGRWSALTPGPPMATAGP-A-DSKTS-NSQLIFAGPKQNGNT-ATVPGTL  556
AAV8 PDB2QA0      LPGPCYRQQRVSTTGQNNNSNF------AWTAGTKYHLNGRNSLANPGIAMATHKDDEER-FFPSNGILIFGKQ-NAARDNAD-YSDV   560

                                        VIII                                                                           βH
AAV9              MITNEEEIKTNPVATESYGQVATNHQSAQAQAQ-TGWVQNQGILPGMVWQDRDVYLQGPIWAKIPHTDGNFHPSPLMGGFGMKHPPPQ  646
AAV2 PDB1LP3      MITDEEEIRTNPVATEQYGSVSTNLQRGNRQAA-TADVNTQGVLPGMVWQDRDVYLQGPIWAKIPHTDGHFHPSPLMGGFGLKHPPPQ  645
AAV4 PDB2G8G      IFTSEEELAATNATDTDMWGNLPGGDQSNS-NLPTVDRLTALGAVPGMVWQNRDIYYQGPIWAKIPHTDGHFHPSPLIGGFGLKHPPPQ  644
AAV8 PDB2QA0      MLTSEEEIKTNPVATEEYGIVADNLQQQNTAPQ-IGTVNSQGALPGMVWQNRDVYLQGPIWAKIPHTDGNFHPSPLMGGFGLKHPPPQ  648

                 βH                            βI                                               IX
AAV9              ILIKNTPVPADPPTAFNKDKLNSFITQYSTGQVSVEIEWELQKENSKRWNPEIQYTSNYYKSNNVEFAVNTEGVYSEPRPIGTRYLTRNL  736
AAV2 PDB1LP3      ILIKNTPVPANPSTTFSAAKFASFITQYSTGQVSVEIEWELQKENSKRWNPEIQYTSNYNKSVNVDFTVDTNGVYSEPRPIGTRYLTRNL  735
AAV4 PDB2G8G      IFIKNTPVPANPPATTFSSTPVNSFITQYSTGQVSVQIDWEIQKERSKRWNPEVQFTSNYGQQNSLLWAPDAAGKYTEPRAIGTRYLTHHL 734
AAV8 PDB2QA0      ILIKNTPVPADPPTTFNQSKLNSFITQYSTGQVSVEIEWELQKENSKRWNPEIQYTSNYYKSTSVDFAVNTEGVYSEPRPIGTRYLTRNL  738
```

FIG 5 Structural alignment of AAV9 VP3 with the VPs of AAV2, AAV4, and AAV8. The VP3 regions from the crystal structures of AAV2, AAV4, AAV8, and AAV9 are compared. Identical residues are shown in white text and a black background, and nonconserved residues are in black with a white background. The eight β-strands that comprise the antiparallel β-barrel motif are depicted with open arrows, the conserved α-helix, αA, is indicated with an open rectangle, and the VR regions are labeled and identified with black arrows. Amino acids in VP regions that are not structurally equivalent to AAV9 are listed in an offset position, below the alignment for each serotype.
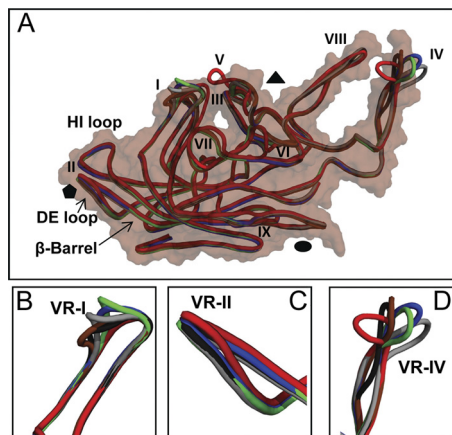
FIG 6 Superposition of AAV VP3 structures. (A) Overlay of the crystal structures of the VP3 monomers of AAV2 (blue), AAV4 (red), AAV8 (green), and AAV9 (brown), with locations of VR-I to VR-IX labeled. The eight-stranded β-barrel motif, DE loop, and HI loop are identified. The approximate locations of some icosahedral symmetry axes are indicated as in Fig. 4A. Panels B, C, and D show close-up views of the superposed structures of AAV2, AAV4, AAV8, and AAV9 for VR-I, VR-II, and VR-IV, respectively. The VR-I, VR-II, and VR-IV conformations as predicted by SWISS MODEL based on the crystal structures of AAV2 and AAV8 and as interactively modeled into the cryo-EM density map are shown in gray and black, respectively, in panels A to D. The images were generated using PyMol (the PyMOL Molecular Graphics System version 1.3, Schrödinger, LLC.).

(AAV9 VP1 numbering) between the viruses. Interestingly, AAV9 amino acids that include residues in VR-IX were identified as the structural determinant of improved melanoma tropism in a chimeric virus, chimeric-1829, which was generated by DNA shuffling approaches (43) from AAV1, AAV2, AAV8, and AAV9. Site-directed mutagenesis confirmed the tissue tropism phenotype of the AAV9 residues, including Trp706, for this chimera, which additionally exhibited altered skeletal muscle, liver, and brain tropism in rodents and nonhuman primates compared to the parental viruses (43). Analysis of chimeric capsids generated between AAV1 and AAV9 also identified a stretch of 113 AAV9 amino acids (aa 456 to 568) within VR-IV to VR-VII as conferring a delayed blood clearance phenotype for AAV9 compared to the other viruses tested, including AAV1, AAV2, and AAV8 (37). In the context of AAV9, the delayed-blood-clearance phenotype was proposed to maintain infectivity in the bloodstream and facilitate enhanced cardiac transduction by this serotype (37). The reported observations on tissue tropism and transduction, combined with the structural differences in the AAV9 VP3 compared to the VPs of AAV2 and AAV8 at VR-I and VR-IV, suggest that these regions and the neighboring residues, including those in VR-V, VR-VIII, and VR-IX, are the probable determinants of AAV9's superior transduction of cardiac and skeletal muscle and liver and pancre-
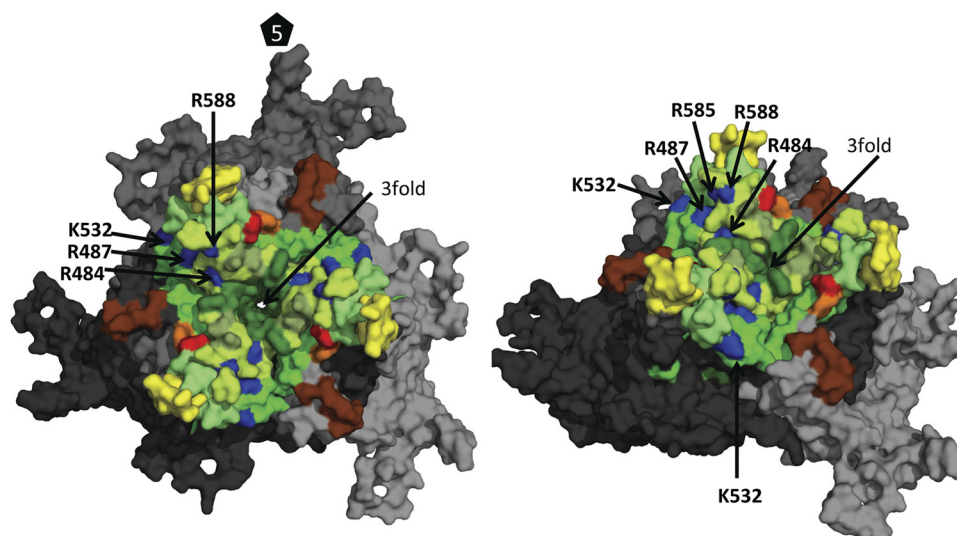
FIG 7 Variable regions of the AAV capsid and associated functions. A trimer of AAV9 VP3 (in black, dark gray, and light gray) is shown viewed down an icosahedral three-fold axis (left) and at a slight rotation (right) with VR-I (brown), VR-IV (yellow), VR-V (lime), and VR-VIII (limon) highlighted. Residue positions equivalent to the heparan sulfate binding site for AAV2 (R484, R487, K532, R585, and R588) are shown in blue. The LamR receptor binding footprint for AAV8, residues equivalent to the amino acids in the two capsid regions aa 489 to 545 and 591 to 621 (AAV9 VP1 numbering), are shown in light and dark green, respectively. Residues 503 (orange) and 504 (purple) are part of the light green LamR footprint. Residues 591 to 594 (gray/green) in the dark green region of the LamR footprint are also part of VR-VIII.

atic tissue compared to AAV1, AAV2, and AAV8 (31, 37, 43, 54, 55, 60, 70).

The detrimental effects on gene therapy trials caused by the presence of preexisting antibodies are well documented (e.g., see references 8, 10, 13, 42, 46, 58, and 65). This underscores the importance of studying the antigenic structures of the AAVs to enable therapeutic vectors to be developed that can escape neutralization. In terms of antigenicity, AAV2 is the best-characterized serotype (13, 44, 58, 74). Thus, a comparative structural analysis of the capsid VRs of AAV2 and AAV9 provides insight into potential AAV9 capsid residues that could be genetically modified to facilitate escape from preexisting host antibody neutralization. Conformational epitopes for three anti-AAV2 capsid antibodies (A20, C37-B, and D3) have been mapped (44, 74). These epitopes vary in their ability to neutralize virus and cross-react with other serotypes. Antibody A20 is specific for AAV2 and AAV3b (44, 74) and binds the epitope that includes residues 263, 264, 272 to 281,

369 to 378, 384, 548, 566 to 575, and 708, which are located in VRs I, III, VII, and IX. This antibody does not bind to AAV9 (data not shown), which is consistent with changes in sequence in the mapped antigenic site (Fig. 5) and with conformational differences in VR-I between AAV2 and AAV9 (Fig. 6B). Interestingly, antibody A20 is reported to neutralize at a postentry event (74). This suggests that either the VRs involved play a role in currently undefined cellular interactions that are inhibited by antibody binding or A20 binding prevents capsid structural transitions required for subsequent steps in infection.

Antibody C37-B only recognizes AAV2, and D3 cross-reacts with AAV1, AAV3, and AAV5 but not AAV4 (74). The peptide-mapped C37-B epitope includes AAV2 residues 493 to 502 and 602 to 610, which are located in VR-V and close to VR-VIII, respectively. Binding by C37-B is neutralizing and inhibits binding to HS (74), the primary receptor for AAV2, which is consistent with the proximity of AAV2 capsid residues, R585 and R588 (VR-

TABLE 3 AAV9 VRs and their reported functional roles

VR	AAV9 aa	Reported functional role(s)	References
VR-I	262–269	Unknown in AAV9	
VR-II	327–332	DE loop at the 5-fold channel; possible role in genome packaging	
VR-III	382–386	Unknown in AAV9	
VR-IV	452–460	aa 456–476, liver transduction efficiency determinant; aa 456-568, delayed blood clearance phenotype	37, 60
VR-V	488–505	aa 489–545 LamR receptor binding footprint; aa 498, 503, and 504, effect on liver- and muscle-specific transduction; aa 456-568, delayed-blood-clearance phenotype	2, 37, 60
VR-VI	527–539	aa 489–545, LamR receptor binding footprint; aa 456-568, delayed-blood-clearance phenotype	2, 37
VR-VII	545–558	aa 550–568, liver transduction efficiency determinant; aa 456-568, delayed blood clearance phenotype	37, 60
VR-VIII	581–593	aa 591–621, LamR receptor binding footprint: aa 582, 590, 592, transduction	2, 60
VR-IX	704–714	aa 699–735, determinant of heart tropism; determinant of improved melanoma tropism in chimeric virus, chimeric-1829; aa 706, mutants exhibited altered tropism	43

VIII) (Fig. 7), critical for the HS interaction (reviewed in reference 1). AAV9 does not differ structurally from AAV2 in VR-VIII, despite sequence differences (Fig. 5), but it does differ at VR-IV, which together with VR-V and VR-VIII form the three-fold protrusion. Consistently, a test of AAV9 capsids against C37-B showed no cross-reactivity (data not shown). The D3 antibody is nonneutralizing, and its epitope contains AAV2 residues 474 to 483, close to VR-V (Fig. 5). These residues occur at the three-fold axis, mostly buried below surface loops, which may explain its nonneutralizing phenotype. The D3 cross-reactivity with AAV1, AAV3, and AAV5, but not AAV4, is consistent with the sequence and structural conservation of the epitope in the viruses recognized and sequence and structural differences in AAV4 at and surrounding this capsid region (27). This antibody was not tested against AAV9, but the anticipation is that it may also cross-react given the similarities in sequence and structure at this capsid region for AAV9 and AAV2 (Fig. 5).

Summary. The ability to visualize the majority of the conserved parvovirus structural features, including the DE loop, HI loop, βBIDG sheet, and αA, as well as two VRs, which exist between all AAV structures determined so far, at the subnanometer resolution of the AAV9 cryo-EM structure, underpins the power of this approach in resolving essential structural features for complex macromolecules to which function can be annotated. The crystal structure provided the atomic context for pinpointing the specific amino acids in the VRs that are important for understanding subtle differences among the AAVs that confer dramatically distinct phenotypes. This information is necessary for generating modified AAV vectors with improved transduction and tissue-specific tropism. Interestingly, the VRs do not appear to be simply involved in initial receptor binding and possibly also facilitate specific postentry interactions with, as yet to be identified, cellular factors. Comparison of AAV9 with AAV2 also identified potential antigenic regions in AAV9 that could be engineered to design a vector that successfully evades capsid-targeted host antibody responses. It is still unknown which AAV9 amino acids dictate the blood-brain-barrier-crossing capabilities of this AAV serotype, although residues in the VRs are likely candidates.

REFERENCES

1. **Agbandje-McKenna M, Kleinschmidt J.** 2011. AAV capsid structure and cell interactions. Methods Mol. Biol. **807:**47–92.
2. **Akache B, et al.** 2006. The 37/67-kilodalton laminin receptor is a receptor for adeno-associated virus serotypes 8, 2, 3, and 9. J. Virol. **80:**9831–9836.
3. **Baker TS, Olson NH, Fuller SD.** 1999. Adding the third dimension to virus life cycles: three-dimensional reconstruction of icosahedral viruses from cryo-electron micrographs. Microbiol. Mol. Biol. Rev. **63:**862–922.
4. **Bell CL, et al.** 2011. The AAV9 receptor and its modification to improve in vivo lung gene transfer in mice. J. Clin. Invest. **121:**2427–2435.
5. **Belnap DM, Kumar A, Folk JT, Smith TJ, Baker TS.** 1999. Low-resolution density maps from atomic models: how stepping "back" can be a step "forward." J. Struct. Biol. **125:**166–175.
6. **Berns KI, Linden RM.** 1995. The cryptic life style of adeno-associated virus. Bioessays **17:**237–245.
7. **Bevan AK, et al.** 2011. Systemic gene delivery in large species for targeting spinal cord, brain, and peripheral tissues for pediatric disorders. Mol. Ther. **19:**1971–1980.
8. **Boutin S, et al.** 2010. Prevalence of serum IgG and neutralizing factors against adeno-associated virus (AAV) types 1, 2, 5, 6, 8, and 9 in the healthy population: implications for gene therapy using AAV vectors. Hum. Gene Ther. **21:**704–712.
9. **Bowman VD, et al.** 2002. An antibody to the putative aphid recognition site on cucumber mosaic virus recognizes pentons but not hexons. J. Virol. **76:**12250–12258.
10. **Brantly ML, et al.** 2009. Sustained transgene expression despite T lymphocyte responses in a clinical trial of rAAV1-AAT gene therapy. Proc. Natl. Acad. Sci. U. S. A. **16:**16363–16368.
11. **Brunger AT.** 1993. Assessment of phase accuracy by cross validation: the free R value. Methods and applications. Acta Crystallogr. D Biol. Crystallogr. **49:**24–36.
12. **Brunger AT, et al.** 1998. Crystallography & NMR system: a new software suite for macromolecular structure determination. Acta Crystallogr. D Biol. Crystallogr. **54:**905–921.
13. **Calcedo R, Vandenberghe LH, Gao G, Lin J, Wilson JM.** 2009. Worldwide epidemiology of neutralizing antibodies to adeno-associated viruses. J. Infect. Dis. **199:**381–390.
14. **Carrillo-Tripp M, et al.** 2009. VIPERdb2: an enhanced and web API enabled relational database for structural virology. Nucleic Acids Res. **37:**D436–D442. doi:10.1093/nar/gkn840.
15. **Chen VB, et al.** 2010. MolProbity: all-atom structure validation for macromolecular crystallography. Acta Crystallogr. D Biol. Crystallogr. **66:**12–21.
16. **Chuah MK, Vandendriessche T.** 2007. Gene therapy for haemophilia "A" and "B": efficacy, safety and immune consequences. Bull. Mem. Acad. R. Med. Belg. **162:**357–361.
17. **Collaborative Computational Project.** 1994. The CCP4 suite: programs for protein crystallography. Acta Crystallogr. D Biol. Crystallogr. **50:**760–763.
18. **Duque S, et al.** 2009. Intravenous administration of self-complementary AAV9 enables transgene delivery to adult motor neurons. Mol. Ther. **17:**1187–1196.
19. **Emsley P, Cowtan K.** 2004. Coot: model-building tools for molecular graphics. Acta Crystallogr. D Biol. Crystallogr. **60:**2126–2132.
20. **Erles K, Sebokova P, Schlehofer JR.** 1999. Update on the prevalence of serum antibodies (IgG and IgM) to adeno-associated virus (AAV). J. Med. Virol. **59:**406–411.
21. **Fechner H, et al.** 2008. Cardiac-targeted RNA interference mediated by an AAV9 vector improves cardiac function in coxsackievirus B3 cardiomyopathy. J. Mol. Med. (Berl.) **86:**987–997.
22. **Fisher KJ, et al.** 1997. Recombinant adeno-associated virus for muscle directed gene therapy. Nat. Med. **3:**306–312.
23. **Flotte TR, Carter BJ.** 1995. Adeno-associated virus vectors for gene therapy. Gene Ther. **2:**357–362.
24. **Foust KD, et al.** 2009. Intravascular AAV9 preferentially targets neonatal neurons and adult astrocytes. Nat. Biotechnol. **27:**59–65.
25. **Fu H, Dirosario J, Killedar S, Zaraspe K, McCarty DM.** 2011. Correction of neurological disease of mucopolysaccharidosis IIIB in adult mice by rAAV9 trans-blood-brain barrier gene delivery. Mol. Ther. **19:**1025–1033.

26. Gao G, et al. 2004. Clades of adeno-associated viruses are widely disseminated in human tissues. J. Virol. 78:6381–6388.

27. Govindasamy L, et al. 2006. Structurally mapping the diverse phenotype of adeno-associated virus serotype 4. J. Virol. 80:11556–11570.

28. Havelka WA, Henderson R, Oesterhelt D. 1995. Three-dimensional structure of halorhodopsin at 7 A resolution. J. Mol. Biol. 247:726–738.

29. Henriques A, et al. 2011. CNS-targeted viral delivery of G-CSF in an animal model for ALS: improved efficacy and preservation of the neuromuscular unit. Mol. Ther. 19:284–292.

30. Hester ME, Foust KD, Kaspar RW, Kaspar BK. 2009. AAV as a gene transfer vector for the treatment of neurological disorders: novel treatment thoughts for ALS. Curr. Gene Ther. 9:428–433.

31. Inagaki K, et al. 2006. Robust systemic transduction with AAV9 vectors in mice: efficient global cardiac gene transfer superior to that of AAV8. Mol. Ther. 14:45–53.

32. Kaya Z, Katus HA, Rose NR. 2010. Cardiac troponins and autoimmunity: their role in the pathogenesis of myocarditis and of heart failure. Clin. Immunol. 134:80–88.

33. Kiefer F, Arnold K, Kunzli M, Bordoli L, Schwede T. 2009. The SWISS-MODEL Repository and associated resources. Nucleic Acids Res. 37:D387–D392. doi:10.1093/nar/gkn750.

34. Klein RL, Dayton RD, Tatom JB, Henderson KM, Henning PP. 2008. AAV8, 9, Rh10, Rh43 vector gene transfer in the rat brain: effects of serotype, promoter and purification method. Mol. Ther. 16:89–96.

35. Kleywegt GJ, Jones TA. 1996. xdlMAPMAN and xdlDATAMAN—programs for reformatting, analysis and manipulation of biomacromolecular electron-density maps and reflection data sets. Acta Crystallogr. D Biol. Crystallogr. 52:826–828.

36. Kontou M, et al. 2005. Structural determinants of tissue tropism and in vivo pathogenicity for the parvovirus minute virus of mice. J. Virol. 79:10931–10943.

37. Kotchey NM, et al. 2011. A potential role of distinctively delayed blood clearance of recombinant adeno-associated virus serotype 9 in robust cardiac transduction. Mol. Ther. 19:1079–1089.

38. Krissinel E, Henrick K. 2004. Secondary-structure matching (SSM), a new tool for fast protein structure alignment in three dimensions. Acta Crystallogr. D Biol. Crystallogr. 60:2256–2268.

39. Kronenberg S, Kleinschmidt JA, Bottcher B. 2001. Electron cryomicroscopy and image reconstruction of adeno-associated virus type 2 empty capsids. EMBO Rep. 2:997–1002.

40. Lei B, Zhang K, Yue Y, Ghosh A, Duan D. 2010. Adeno-associated virus serotype-9 mediated retinal outer plexiform layer transduction is mainly through the photoreceptors. Adv. Exp. Med. Biol. 664:671–678.

41. Lerch TF, Xie Q, Chapman MS. 2010. The structure of adeno-associated virus serotype 3B (AAV-3B): insights into receptor binding and immune evasion. Virology 403:26–36.

42. Li C, et al. 2012. Neutralizing antibodies against adeno-associated virus examined prospectively in pediatric patients with hemophilia. Gene Ther. 19:288–294.

43. Li W, et al. 2008. Engineering and selection of shuffled AAV genomes: a new strategy for producing targeted biological nanoparticles. Mol. Ther. 16:1252–1260.

44. Lochrie MA, et al. 2006. Mutations on the external surfaces of adeno-associated virus type 2 capsids that affect transduction and neutralization. J. Virol. 80:821–834.

45. McCown TJ. 2011. Adeno-associated virus (AAV) vectors in the CNS. Curr. Gene Ther. 11:181–188.

46. McPhee SW, et al. 2006. Immune responses to AAV in a phase I study for Canavan disease. J. Gene Med. 8:577–588.

47. Miller EB, et al. 2006. Production, purification and preliminary X-ray crystallographic studies of adeno-associated virus serotype 1. Acta Crystallogr. Sect. F Struct. Biol. Cryst. Commun. 62:1271–1274.

48. Mitchell M, et al. 2009. Production, purification and preliminary X-ray crystallographic studies of adeno-associated virus serotype 9. Acta Crystallogr. Sect. F Struct. Biol. Cryst. Commun. 65:715–718.

49. Muzyczka N, Berns K. (ed). 2001. Parvoviridae: the viruses and their replication, 4th ed. Lippincott Williams & Wilkins, New York, NY.

50. Nam HJ, et al. 2011. Structural studies of adeno-associated virus serotype 8 capsid transitions associated with endosomal trafficking. J. Virol. 85:11791–11799.

51. Nam HJ, et al. 2007. Structure of adeno-associated virus serotype 8, a gene therapy vector. J. Virol. 81:12260–12271.

52. Navaza J. 2001. Implementation of molecular replacement in AMoRe. Acta Crystallogr. D Biol. Crystallogr. 57:1367–1372.

53. Ng R, et al. 2010. Structural characterization of the dual glycan binding adeno-associated virus serotype 6. J. Virol. 84:12945–12957.

54. Pacak CA, Byrne BJ. 2011. AAV vectors for cardiac gene transfer: experimental tools and clinical opportunities. Mol. Ther. 19:1582–1590.

55. Pacak CA, et al. 2006. Recombinant adeno-associated virus serotype 9 leads to preferential cardiac transduction in vivo. Circ. Res. 99:e3–e9. doi:10.1161/01.RES.0000237661.18885.f6.

56. Padron E, et al. 2005. Structure of adeno-associated virus type 4. J. Virol. 79:5047–5058.

57. Parrish CR. 2010. Structures and functions of parvovirus capsids and the process of cell infection. Curr. Top. Microbiol. Immunol. 343:149–176.

58. Peden CS, Burger C, Muzyczka N, Mandel RJ. 2004. Circulating anti-wild-type adeno-associated virus type 2 (AAV2) antibodies inhibit recombinant AAV2 (rAAV2)-mediated, but not rAAV5-mediated, gene transfer in the brain. J. Virol. 78:6344–6359.

59. Pettersen EF, et al. 2004. UCSF Chimera—a visualization system for exploratory research and analysis. J. Comput. Chem. 25:1605–1612.

60. Pulicherla N, et al. 2011. Engineering liver-detargeted AAV9 vectors for cardiac and musculoskeletal gene transfer. Mol. Ther. 19:1070–1078.

61. Rabinowitz JE, et al. 2004. Cross-dressing the virion: the transcapsidation of adeno-associated virus serotypes functionally defines subgroups. J. Virol. 78:4421–4432.

62. Rabinowitz JE, et al. 2002. Cross-packaging of a single adeno-associated virus (AAV) type 2 vector genome into multiple AAV serotypes enables transduction with broad specificity. J. Virol. 76:791–801.

63. Rosenthal PB, Henderson R. 2003. Optimal determination of particle orientation, absolute hand, and contrast loss in single-particle electron cryomicroscopy. J. Mol. Biol. 333:721–745.

64. Sarkar R, et al. 2006. Long-term efficacy of adeno-associated virus serotypes 8 and 9 in hemophilia A dogs and mice. Hum. Gene Ther. 17:427–439.

65. Scallan CD, et al. 2006. Human immunoglobulin inhibits liver transduction by AAV vectors at low AAV2 neutralizing titers in SCID mice. Blood 107:1810–1817.

66. Schwede T, Kopp J, Guex N, Peitsch MC. 2003. SWISS-MODEL: an automated protein homology-modeling server. Nucleic Acids Res. 31:3381–3385.

67. Sharma A, Tovey JC, Ghosh A, Mohan RR. 2010. AAV serotype influences gene transfer in corneal stroma in vivo. Exp. Eye Res. 91:440–448.

68. Shen S, Bryant KD, Brown SM, Randell SH, Asokan A. 2011. Terminal N-linked galactose is the primary receptor for adeno-associated virus 9. J. Biol. Chem. 286:13532–13540.

69. Suckau L, et al. 2009. Long-term cardiac-targeted RNA interference for the treatment of heart failure restores cardiac function and reduces pathological hypertrophy. Circulation 119:1241–1252.

70. Sun B, et al. 2008. Correction of multiple striated muscles in murine Pompe disease through adeno-associated virus-mediated gene therapy. Mol. Ther. 16:1366–1371.

71. Vandendriessche T, et al. 2007. Efficacy and safety of adeno-associated viral vectors based on serotype 8 and 9 vs. lentiviral vectors for hemophilia B gene therapy. J. Thromb. Haemost. 5:16–24.

72. Walters RW, et al. 2004. Structure of adeno-associated virus serotype 5. J. Virol. 78:3361–3371.

73. Weitzman MD, Linden RM. 2011. Adeno-associated virus biology. Methods Mol. Biol. 807:1–23.

74. Wobus CE, et al. 2000. Monoclonal antibodies against the adeno-associated virus type 2 (AAV-2) capsid: epitope mapping and identification of capsid domains involved in AAV-2-cell interaction and neutralization of AAV-2 infection. J. Virol. 74:9281–9293.

75. Wriggers W. 2010. Using Situs for the integration of multi-resolution structures. Biophys. Rev. 2:21–27.

76. Xiao W, et al. 1999. Gene therapy vectors based on adeno-associated virus type 1. J. Virol. 73:3994–4003.

77. Xiao X, Li J, Samulski RJ. 1996. Efficient long-term gene transfer into muscle tissue of immunocompetent mice by adeno-associated virus vector. J. Virol. 70:8098–8108.

78. Xie Q, et al. 2002. The atomic structure of adeno-associated virus (AAV-2), a vector for human gene therapy. Proc. Natl. Acad. Sci. U. S. A. 99:10405–10410.

79. Xie Q, Lerch TF, Meyer NL, Chapman MS. 2011. Structure-function analysis of receptor-binding in adeno-associated virus serotype 6 (AAV-6). Virology 420:10–19.

80. **Xue YQ, et al.** 2010. AAV9-mediated erythropoietin gene delivery into the brain protects nigral dopaminergic neurons in a rat model of Parkinson's disease. Gene Ther. **17:**83–94.

81. **Yan X, Dryden KA, Tang J, Baker TS.** 2007. Ab initio random model method facilitates 3D reconstruction of icosahedral particles. J. Struct. Biol. **157:**211–225.

82. **Yan X, Sinkovits RS, Baker TS.** 2007. AUTO3DEM—an automated and high throughput program for image reconstruction of icosahedral particles. J. Struct. Biol. **157:**73–82.

83. **Zhang X, Walker SB, Chipman PR, Nibert ML, Baker TS.** 2003. Reovirus polymerase lambda 3 localized by cryo-electron microscopy of virions at a resolution of 7.6 A. Nat. Struct. Biol. **10:**1011–1018.